Supplementary Information (SI) for Dalton Transactions.

Electronic Supplementary Information

In situ Formation of an Active Oxygen Evolution Catalyst *via* Photodegradation of $[Ru(bpy)_3]^{2+}$

Marcel Langer,[a,b] Alexander K. Mengele,[b] Riccarda Müller,[b] Julius C. Wetzel,[a] Judith Mayer,[b] Sven Rau,*,[b] and Carsten Streb*,[a,b]

Table of Contents

1. Instrumentation 2
2. Experimental procedures 3
3. Influence of irradiation 6
4. Influence of the SOA concentration 6
5. Reference experiments 7
6. *Operando* UV-Vis studies 8
    a) Typical light-induced OER of the prototype system 8
    b) Typical light-induced OER of the prototype system under diluted conditions 9
    c) UV-Vis spectrum of the isolated green oily deposit obtained after a typical light-induced OER experiment 10
7. Influence of the solvent and solvent ratio in photocatalytic OER experiments 11
8. Effect of additional bipyridine (bpy) 12
    a) *Operando* UV-Vis study in the presence of 10 mM bpy 12
    b) O_2 quantification in photocatalytic OER experiments in the presence of additional bpy 13
    c) ATR-FTIR characterization of the colorless precipitate obtained after a photocatalytic OER experiment in the presence of additional bpy 13
9. Different ruthenium polypyridyl-based PS 14
10. Structural characterization data for ipphCOOH and PS4 16
11. Control experiment in purely aqueous media 21
12. Literature 22

1. Instrumentation

Attenuated total reflectance-Fourier-transform infrared spectroscopy (ATR-FTIR) was performed on a Bruker Alpha II equipped with an ATR Platinum Diamond unit. The data were recorded with 24 scans at a resolution of 4 cm^{-1}.

Operando **UV-Vis absorbance spectroscopy** was performed on an Avantes AvaSpec-ULS2048CL detector unit coupled with an AVA AvaLight-DH-S-BAL light source. The light source, cuvette holder and detector were connected within the system *via* fiber optic cables. Standard quartz glass screw top emission cuvettes (d = 10.0 mm) were used for all inert *operando* UV-Vis measurements. At the beginning, UV-Vis spectra were recorded every second (in the case of the standard experiment 5 s) and after an appropriate time every 3 min (in the case of the standard experiment 5 min). The first 5 min of each measurement were carried out in the dark, followed by irradiation of the homogeneous solutions with blue LED light (λ_{max} = 470 nm, power density: *ca.* 50 mW cm^{-2}).

NMR spectra were recorded either on a Bruker Avance 400 MHz, a Bruker Avance 500 MHz or a Bruker Avance Neo 400 MHz. All spectra were measured at room temperature unless otherwise noted and referenced to the solvent residual peaks (2.50 ppm (quintet, ^{1}H-spectra) or 39.52 ppm (septet, ^{13}C-spectra) for DMSO-d_6; 1.94 ppm (quintet, ^{1}H-spectra) or 1.32 ppm (singlet, ^{13}C-spectra) for MeCN-d_3).

High resolution mass spectrometry (HRMS) was performed using a Fourier Transform Ion Cyclotron Resonance (FT-ICR) mass spectrometer solariX (Bruker Daltonics) equipped with a 7.0 T superconducting magnet and interfaced to an Apollo II Dual ESI/MALDI source. For all MALDI measurements *trans*-2-[3-(4-*tert*-butylphenyl)-2-methyl-2-propenylidene]malononitrile (DCTB) was used as matrix. Spectra were analyzed with the DataAnalysisViewer 4.2 from Bruker and transferred to Origin 2023b. Spectra simulation was performed with mMass Version 5.5.0 and transferred to Origin 2023b as well.

2. Experimental procedures

Chemicals: [Ru(bpy)$_3$](PF$_6$)$_2$ (PS1a), $Na_2S_2O_8$, acetonitrile (MeCN for HPLC; gradient grade ≥99.9%), *N,N*`-dimethylformamide (DMF for HPLC; gradient grade ≥99.9%), acetone and bipyridine (bpy) used for oxygen evolution reaction experiments as well as all chemicals used for synthesis in this work were purchased commercially from Sigma Aldrich Chemical Company LTD., Acros Organics B.V.B.A., Carl Roth GmbH & Co. KG and ABCR GmbH & Co. KG and were of reagent grade. The chemicals were used without further purification unless otherwise stated. Purified water in terms of Milli-Q-water (resistivity: 18.2 MΩcm at 298.15 K; Millipore) was used for all studies.

Ligand abbreviations: bpy = 2,2´-bipyridine; tbbpy = 4,4´-di-*tert*-butyl-2,2´-bipyridine; phen = 1,10-phenanthroline; dppz = dipyrido[3,2-*a*:2´,3´-*c*] phenazine; *p*-tolbip = 1-(4-methylphenyl)-3-benzyl-1*H*-imidazo[4,5-*f*][1,10] phenanthroline; ipphCOOH = 4-(1*H*-imidazol[4,5-*f*][1,10]phenanthroline-2-yl)benzoic acid.

Synthesis: 1,10-phenanthroline-5,6-dione,[1] [RuCl$_2$(tbbpy)$_2$][2] and [Ru(tbbpy)$_2$(*p*-tolbip)](PF$_6$)$_2$ (PS3)[3] were synthesized according to literature. [Ru(tbbpy)$_3$](PF$_6$)$_2$ (PS1b), [Ru(tbbpy)$_2$(phen)](PF$_6$)$_2$ (PS2) and [Ru(tbbpy)$_2$(dppz)](PF$_6$)$_2$ (PS5) were synthesized according to literature[4] with precipitation of the obtained Cl-containing complex by aqueous NH_4PF_6 solution.

ipphCOOH was synthesized by combining 700.2 mg 1,10-phenathroline-5,6-dione (3.33 mmol, 1.00 eq.), 501.0 mg 4-formyl benzoic acid (3.33 mmol, 1.00 eq.) and 3060 mg (39.7 mmol, 11.9 eq.) ammonium acetate in a 250 mL one-necked round bottom flask. Subsequently, 22 mL acetic acid was added to the flask and the mixture was heated inside a microwave for 30 min with 350 W under vigorous stirring. After cooling to room temperature, the yellow product was collected by filtration and washed several times with water and diethyl ether each. After collection of the yellow solid, it was dried at elevated temperatures (*ca.* 50 °C) under vacuum to yield 1.071 g (3.14 mmol, 94%) of the product, which is well soluble in DMSO.

^{1}H-NMR (400 MHz, r.t., DMSO-d$_6$): δ 13.86 (broad s, 1H), 9.04 – 9.00 (m, 2H), 8.89 (d, J = 8.1 Hz, 2H), 8.37 (d, J = 8.2 Hz, 2H), 8.16 (d, J = 8.3 Hz, 2H), 7.81 (dd, J = 7.7, 4.2 Hz, 2H).

^{13}C-NMR (101 MHz, r.t., DMSO-d$_6$): δ 172.13, 167.07, 149.49, 148.08, 143.79, 133.69, 131.53, 130.10, 129.78, 126.20, 123.42.

[Ru(tbbpy)$_2$(ipphCOOH)](PF$_6$)$_2$ (**PS4**) was synthesized as follows: In a 250 mL one-necked round bottom flask 200.5 mg [(tbbpy)$_2$RuCl$_2$] (0.283 mmol, 1.00 eq.) and 107.2 mg ipphCOOH (0.315 mmol, 1.10 eq.) were dispersed in a mixture of 60 mL EtOH and 20 mL H_2O. The suspension was refluxed for 18 h at 85 °C thereby forming a clear red solution. After removal of EtOH by rotary evaporation, the crude product was precipitated by the addition of a solution of 585 mg NH_4PF_6 dissolved in 10 mL water. Upon filtering off the obtained solid and washing the crude product several times with water and diethyl ether, the red solid was dissolved in DCM, filtered again through celite and then the solvent was removed in vacuo. Finally, 311 mg of the product were obtained (0.246 mmol, 87%).

^{1}H-NMR (500 MHz, 340 K, MeCN-d$_3$): δ 8.91 (d, J = 8.0 Hz, 2H), 8.53 (d, J = 1.8 Hz, 2H), 8.49 (d, J = 1.7 Hz, 2H), 8.23 (d, J = 6.3 Hz, 2H), 8.11 (d, J = 6.8 Hz, 2H), 7.96 (d, J = 5.1 Hz, 2H), 7.73 – 7.67 (m, 2H), 7.53 (d, J = 5.7 Hz, 2H), 7.49 (dd, J = 6.0, 2.0 Hz, 2H), 7.30 – 7.20 (m, 2H), 1.47 (s, 18H), 1.37 (s, 18H).

^{13}C-NMR (101 MHz, r.t., MeCN-d$_3$ + TFA): δ 166.71, 164.07, 163.94, 158.05, 157.88, 153.98, 152.36, 152.10, 150.67, 148.45, 135.88, 132.17, 131.81, 129.72, 128.32, 128.17, 127.20, 125.83, 125.57, 122.72, 122.64, 121.88, 36.47, 36.37, 30.56, 30.46.

HRMS (MALDI-FT-ICR; [M] = $C_{56}H_{60}F_{12}N_8O_2P_2Ru$): calcd. for $[M\text{-}2PF_6\text{-}H]^+$ 977.3817, found 977.3821; calcd. for $[M\text{-}PF_6]^+$ 1123.3546, found 1123.3541; calcd. for $[2M\text{-}2PF_6\text{-}H]^+$ 2245.7018, found 2245.7081; calcd. for $[2M\text{-}PF_6]^+$ 2391.6738, found 2391.6710; calcd. for $[3M\text{-}2PF_6\text{-}H]^+$ 3514.0214, found 3514.0305; calcd. for $[3M\text{-}PF_6\text{-}H]^+$ 3658.9856, found 3659.0278.

All high-resolution MS data and NMR data for the structural characterization of ipphCOOH and $[Ru(tbbpy)_2(ipphCOOH)](PF_6)_2$ are provided in chapter 10 of this document.

Oxygen detection: *FireStingO2 optical oxygen meter* (Pyroscience, Germany) and oxygen-sensitive optical sensor spots (*OXSP5*, with optical isolation) were used for the simultaneous quantification of oxygen in the solution and gas phase. The sensor spots were glued to the inner glass wall of a screw-capped, hermetically sealed vial using a transparent silicone glue (*SPGLUE*). Each sensor spot was calibrated separately by a two-point calibration. The O_2 sensor in the gas phase was calibrated against ambient air and argon atmosphere. The sensor in solution was calibrated against the deaerated and untreated, air-equilibrated solvent mixture MeCN/H_2O (9:1, v/v). Prior to light-driven OER studies with different solvents, the sensor spots were recalibrated to the respective solvent mixture. The molar amount of oxygen was calculated based on the molar amounts of oxygen detected in the solution (in µM) and *via* the ideal gas equation ($c = p R^{-1} T^{-1}$) for the oxygen partial pressure determined in the gas phase (in mbar). The total amounts of O_2 were calculated using the following equation: $((c_{\text{gas}}V_{\text{gas}})(c_{\text{solution}}V_{\text{solution}}))\ V_{\text{total}}^{-1}$. For further details on the oxygen sensor equipment and the O_2 quantification set up, the reader is referred to the literature provided by Streb, Rau and co-workers.[5]

Typical light-driven OER experiments: 5 mL deaerated MeCN/H_2O (9:1, v/v) containing 1 mM of the respective PS and 10 mM $Na_2S_2O_8$ were prepared under an inert atmosphere and in the exclusion of light. A hermetically sealed vial (diameter: 12.75 ± 0.25 mm, length: 99.00 ± 0.50 mm) equipped with two fiber-optic fluorescent oxygen sensor spots was used as the reaction vessel. The vial was mounted in a custom-built air-cooled photoreactor (≈ 298 K), and oxygen was detected *in operando* in the solution and in the gas phase (see Figure S1). The first 5 min of each measurement were performed in the dark, followed by irradiation of the homogeneous solutions with blue LED light (λ_{max} = 470 nm, power density: *ca.* 50 mW cm^{-2}). The photocatalytic OER experiments were conducted under moderate magnetic stirring (250 rpm).

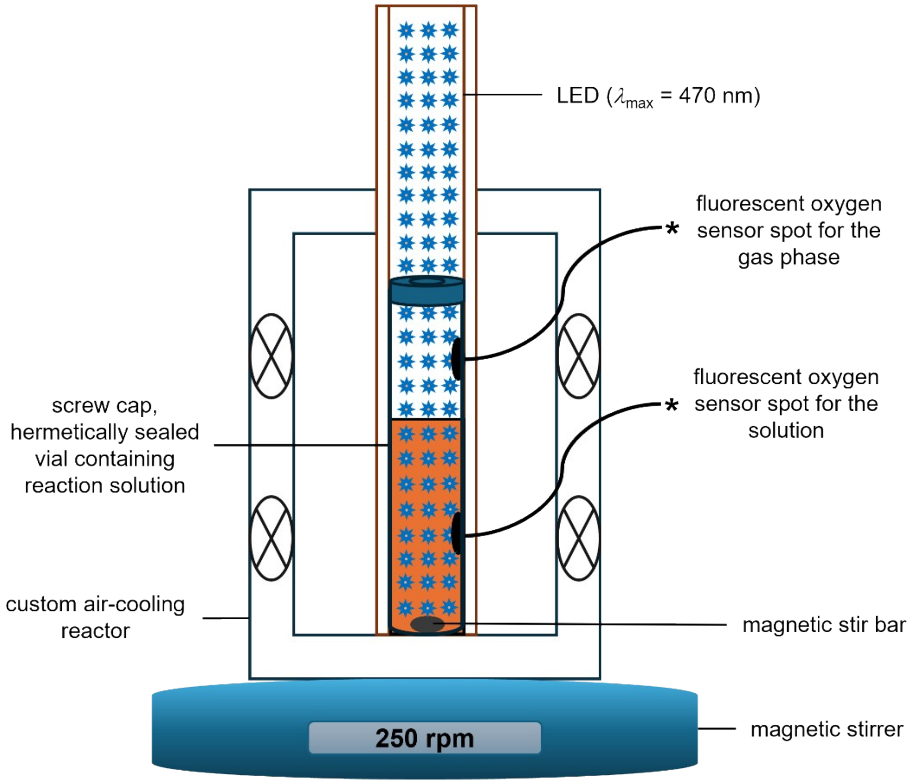

Figure S1: Schematic illustration of the setup used for light-driven OER studies. O_2 evolution was quantified *in operando* in a custom-built air-cooled photoreactor *via* fiber-optic fluorescent oxygen sensor spots in the solution and the gas phase simultaneously.

3. Influence of irradiation

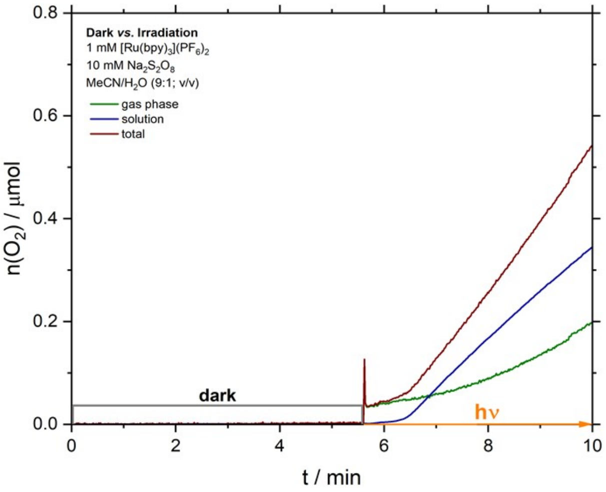

Figure S2: Light-driven OER profile in the gas phase (green), in solution (blue) and in total (red) using LED light (λ_{max} = 470 nm, power density: *ca*. 50 mW cm^{-2}): Negligible amount of O_2 under dark conditions for *t* = 0-5 min and strong O_2 evolution upon irradiation, providing evidence for the necessity of photons (*t* > 5 min) to operate light-driven oxygen evolution by the prototype OER system with $[Ru(bpy)_3](PF_6)_2$ (1 mM) and $Na_2S_2O_8$ (10 mM) in $MeCN/H_2O$ (9:1, v/v).

4. Influence of the SOA concentration

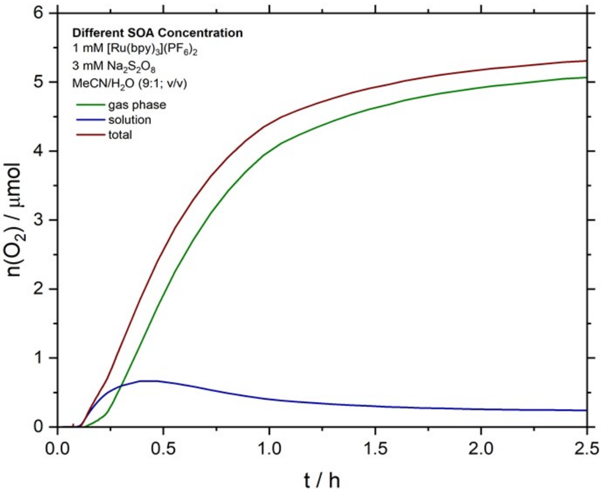

Figure S3: Influence of the SOA concentration on the amount of O_2 evolved during light-driven OER in the gas phase (green), in solution (blue) and in total (red) using $[Ru(bpy)_3](PF_6)_2$ (1 mM) and $Na_2S_2O_8$ (3 mM) in $MeCN/H_2O$ (9:1, v/v); LED light (λ_{max} = 470 nm, power density: *ca*. 50 mW cm^{-2}): Significantly reduced O_2 evolution upon irradiation indicates a stoichiometric equivalence between oxygen evolved and oxidation equivalents from the SOA.

5. Reference experiments

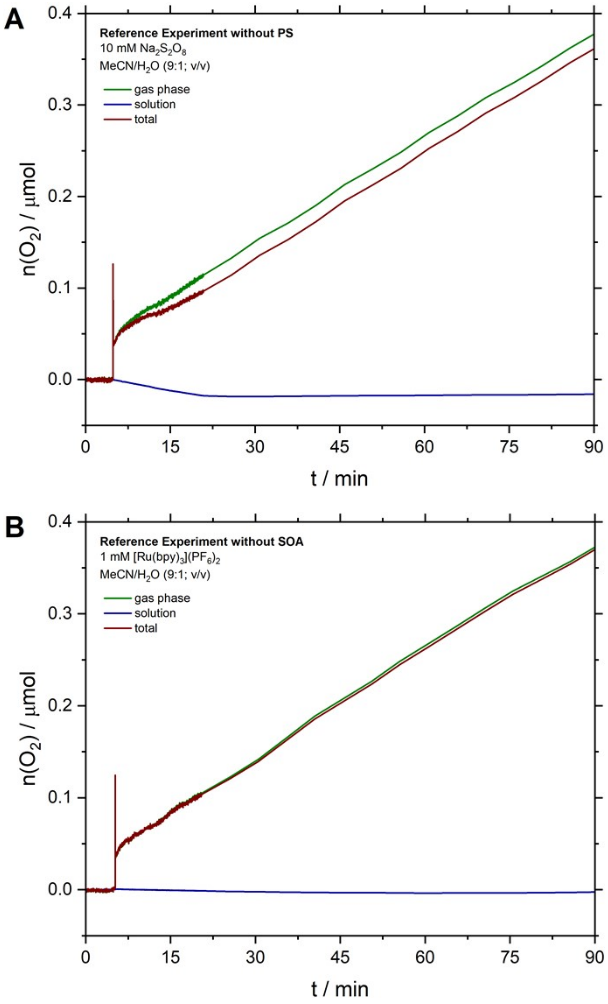

Figure S4: Reference measurements and their light-driven OER profiles in the gas phase (green), in solution (blue) and in total (red) using LED light (λ_{max} = 470 nm, power density: *ca*. 50 mW cm^{-2}): **A)** Negligible O_2 evolution upon irradiation of a PS-free solution containing only $Na_2S_2O_8$ (10 mM) in MeCN/H_2O (9:1, v/v). **B)** Negligible O_2 evolution upon irradiation of an SOA-free solution containing only $[Ru(bpy)_3](PF_6)_2$ (1 mM) in MeCN/H_2O (9:1, v/v). Note that the blue LED might have a significant influence on the detection response of the oxygen sensor spots, resulting in a light-induced signal drift for the gas phase (green curve) and a decreasing signal intensity below zero for the solution (blue curve), as can be observed in both figure panels A and B.

6. *Operando* UV-Vis studies

a) Typical light-induced OER of the prototype system

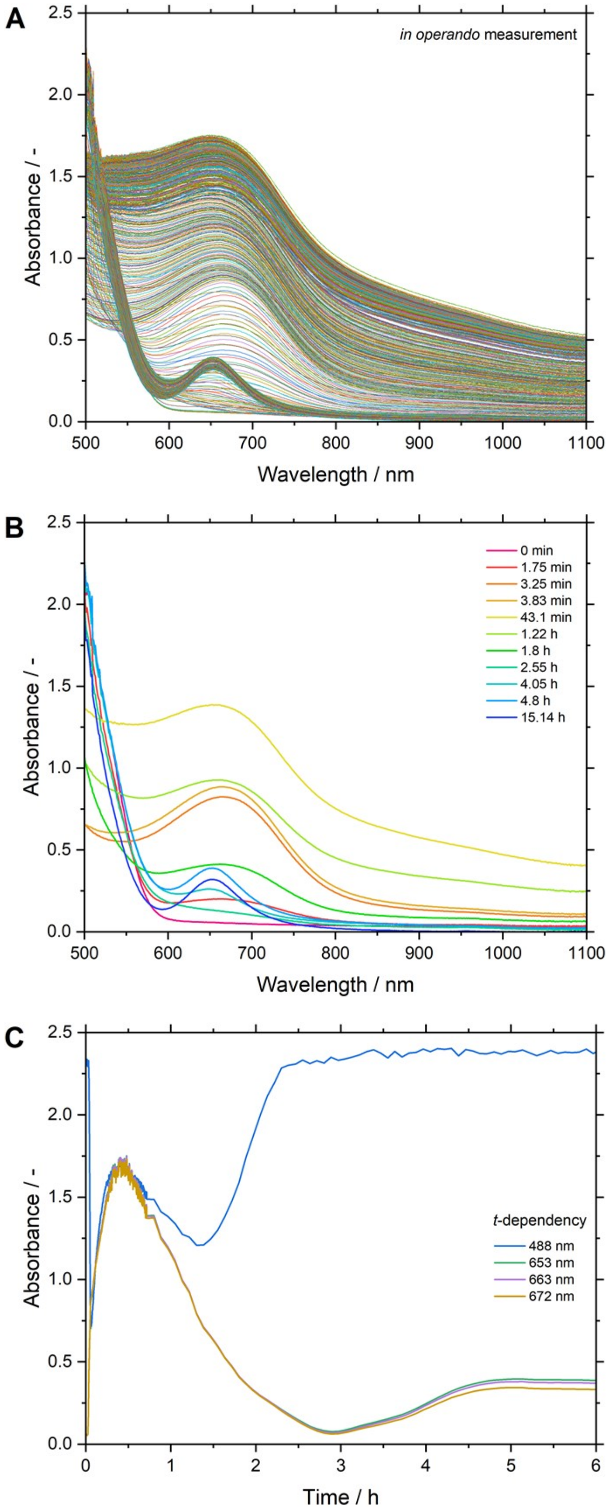

Figure S5: *Operando* UV-Vis spectra of the prototype light-driven OER system with $[Ru(bpy)_3](PF_6)_2$ (1 mM) and $Na_2S_2O_8$ (10 mM) in $MeCN/H_2O$ (9:1, v/v) using LED light (λ_{max} = 470 nm, power density: *ca*. 50 mW cm^{-2}): **A)** Common representation of all UV-Vis spectra recorded in the experiment. **B)** Change of the UV-Vis spectrum on a selected time scale of the entire UV-Vis spectrum above. **C)** Time-dependent change of selected electronic transition bands.

b) Typical light-induced OER of the prototype system under diluted conditions

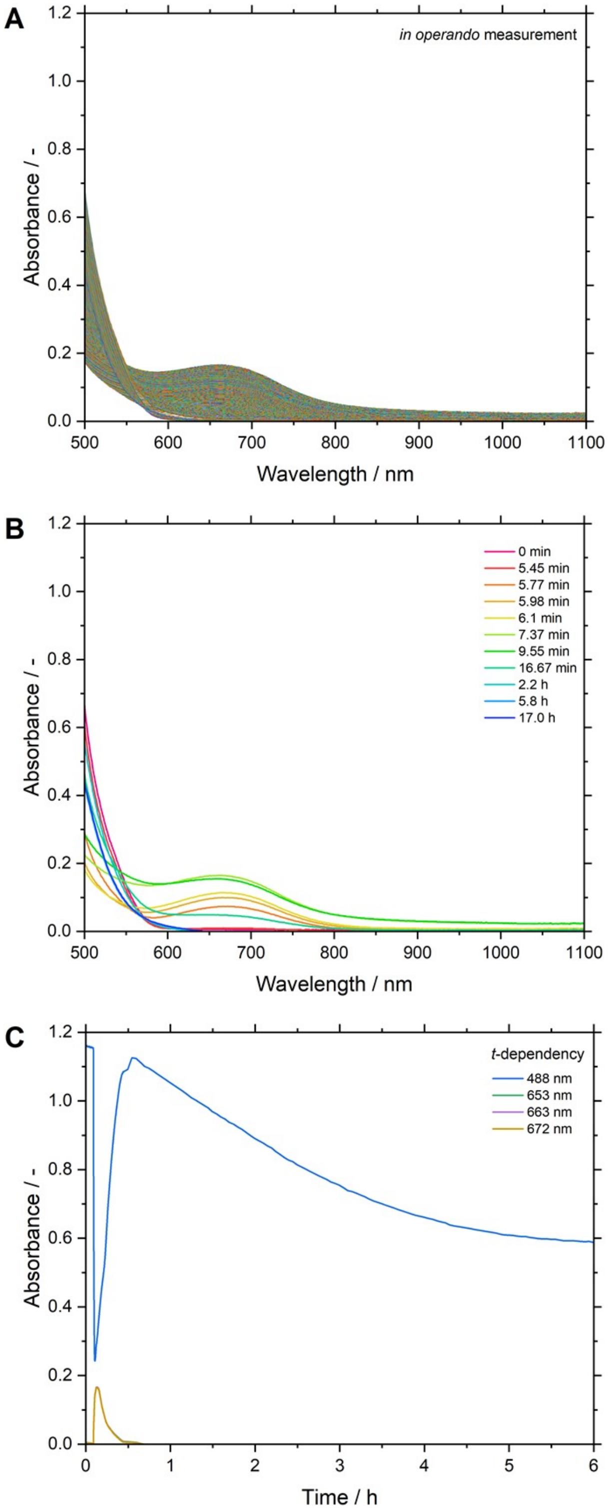

Figure S6: *Operando* UV-Vis spectra of the prototype light-driven OER system under diluted conditions with $[Ru(bpy)_3](PF_6)_2$ (0.1 mM) and $Na_2S_2O_8$ (1 mM) in $MeCN/H_2O$ (9:1, v/v) using LED light (λ_{max} = 470 nm, power density: *ca*. 50 mW cm^{-2}): **A)** Common representation of all UV-Vis spectra recorded in the experiment. **B)** Change of the UV-Vis spectrum on a selected time scale of the entire UV-Vis spectrum above. **C)** Time-dependent change of selected electronic transition bands.

c) UV-Vis spectrum of the isolated green oily deposit obtained after a typical light-induced OER experiment

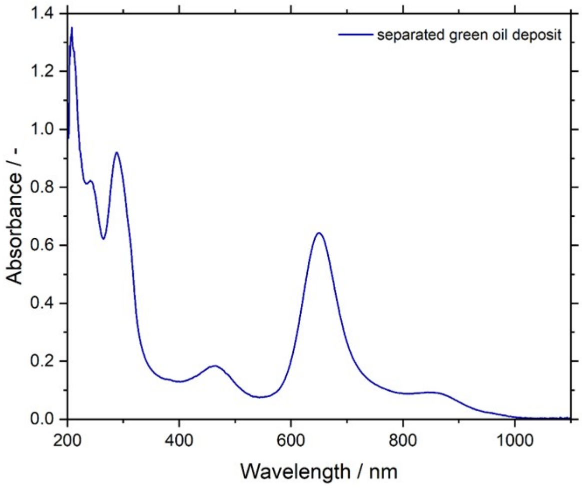

Figure S7: UV-Vis spectrum of the separated green oily deposit obtained after typical light-driven OER of the prototype OER system. Electronic transitions at 464 nm and 650 nm indicate the simultaneous formation of both orange Ru_2(III,IV) and blue Ru_2(III,III) PS dimers.[6] Further electronic transitions can be observed at 208 nm and 288 nm (LC, $\pi\pi^*_{bpy}$), 242 nm (MLCT) and two shoulders at 383 nm and 854 nm (dπdπ).

7. Influence of the solvent and solvent ratio in photocatalytic OER experiments

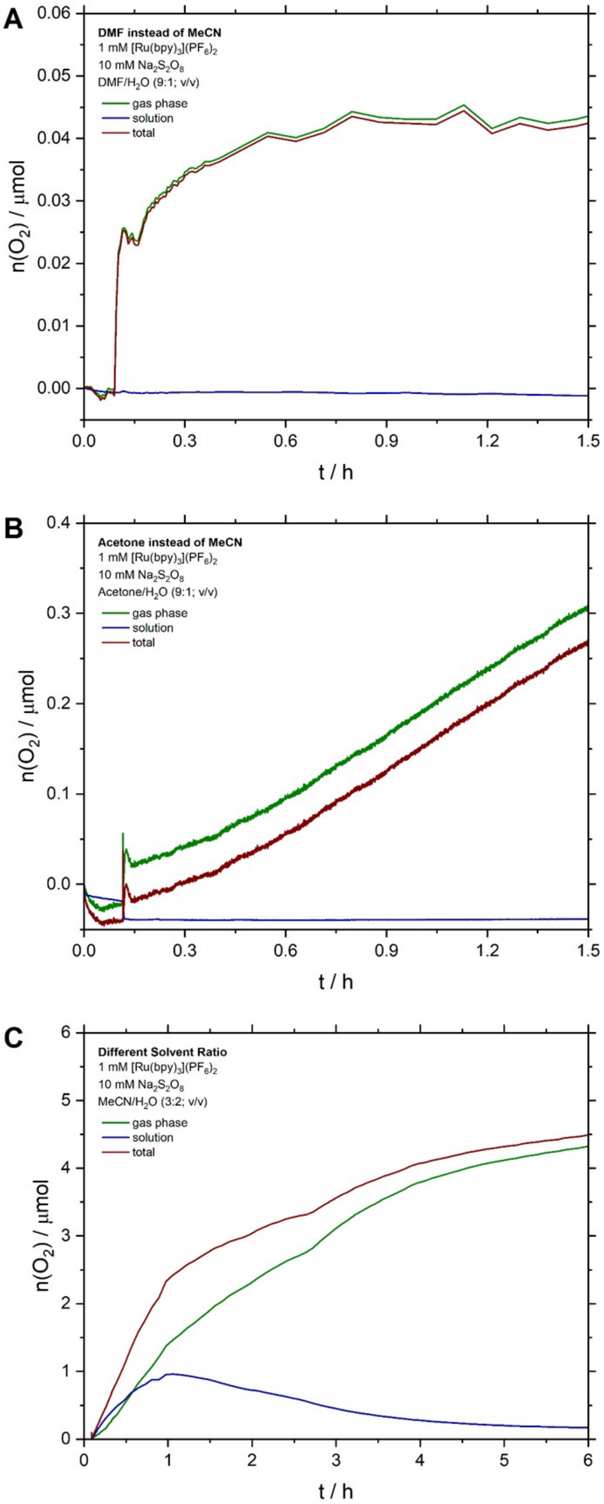

Figure S8: Influence of the solvent and solvent ratio on the amount of O_2 evolved during light-driven OER in the gas phase (green), in solution (blue) and in total (red) under the following conditions: $[Ru(bpy)_3](PF_6)_2$ (1 mM) and $Na_2S_2O_8$ (10 mM) in X/H_2O (9:1, v/v) using LED light (λ_{max} = 470 nm, power density: *ca*. 50 mW cm^{-2}): **A)** Negligible O_2 evolution upon irradiation for X = DMF. **B)** Negligible O_2 evolution upon irradiation for X = acetone. **C)** Significantly reduced O_2 evolution upon irradiation using an increased water content with MeCN/H_2O 3:2 (v/v). Note that the blue LED might have a significant influence on the detection response of the oxygen sensor spots, resulting in a light-induced signal drift for the gas phase (green curve) and a decreasing signal intensity below zero for the solution (blue curve), as can be observed in the figure panels A and B.

8. Effect of additional bipyridine (bpy)

a) *Operando* UV-Vis study in the presence of 10 mM bpy

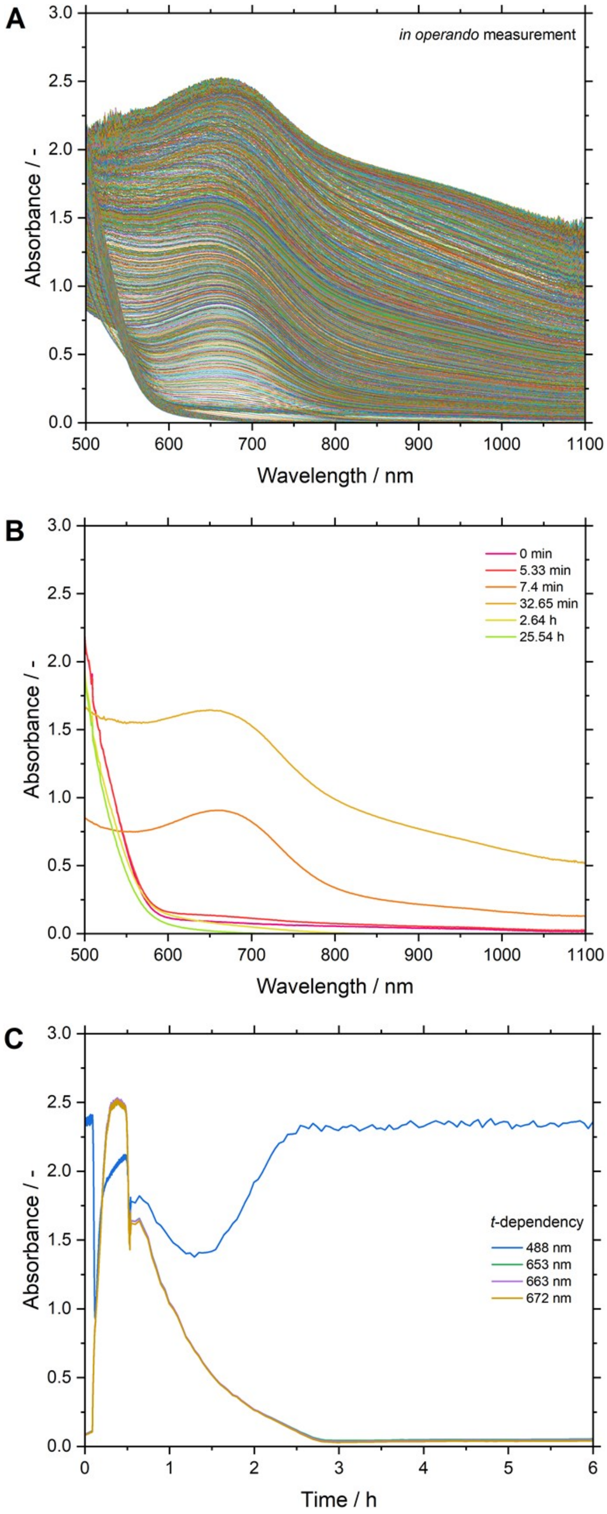

Figure S9: *Operando* UV-Vis spectra showing the effect of additional ligand bpy (10 mM) on the prototype light-driven OER system with $[Ru(bpy)_3](PF_6)_2$ (1 mM) and $Na_2S_2O_8$ (10 mM) in $MeCN/H_2O$ (9:1, v/v) using LED light (λ_{max} = 470 nm, power density: *ca*. 50 mW cm^{-2}): **A)** Common representation of all UV-Vis spectra recorded in the experiment. **B)** Change of the UV-Vis spectrum on a selected time scale of the entire UV-Vis spectrum above. **C)** Time-dependent change of selected electronic transition bands.

b) O_2 quantification in photocatalytic OER experiments in the presence of additional bpy

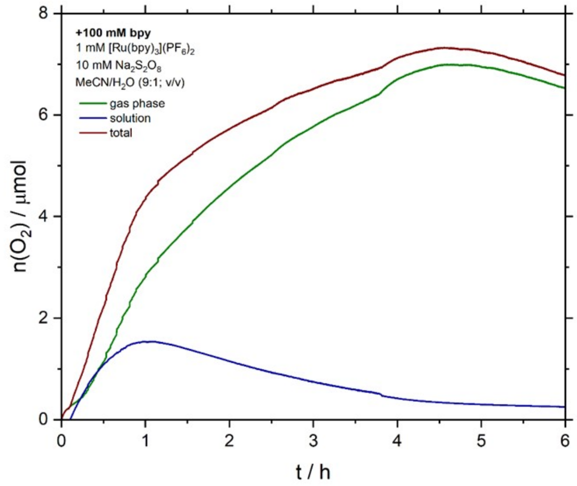

Figure S10: Light-driven OER profile in the gas phase (green), in solution (blue) and in total (red) showing the effect of the additional ligand bpy on the O_2 evolution of the prototype light-driven OER system with $[Ru(bpy)_3](PF_6)_2$ (1 mM) and $Na_2S_2O_8$ (10 mM) in MeCN/H_2O (9:1, v/v) using LED light (λ_{max} = 470 nm, power density: *ca*. 50 mW cm^{-2}). Additional 100 mM bpy results in a significantly reduced amount of O_2 evolved during irradiation.

c) ATR-FTIR characterization of the colorless precipitate obtained after a photocatalytic OER experiment in the presence of additional bpy

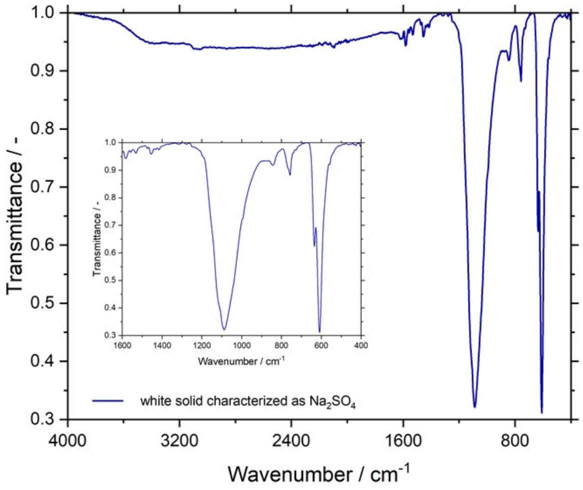

Figure S11: ATR-FTIR spectrum of the separated colorless solid that was obtained after light-driven OER catalysis in the presence of additional 100 mM bpy (conditions: 1 mM $[Ru(bpy)_3](PF_6)_2$, 10 mM $Na_2S_2O_8$, MeCN/H_2O 9:1 (v/v), LED light with λ_{max} = 470 nm and power density *ca*. 50 mW cm^{-2}). Characteristic IR vibrational modes at 1087 cm^{-1}, 635 cm^{-1} and 610 cm^{-1} indicate the formation of sodium sulfate (Na_2SO_4).[7]

9. Different ruthenium polypyridyl-based PS

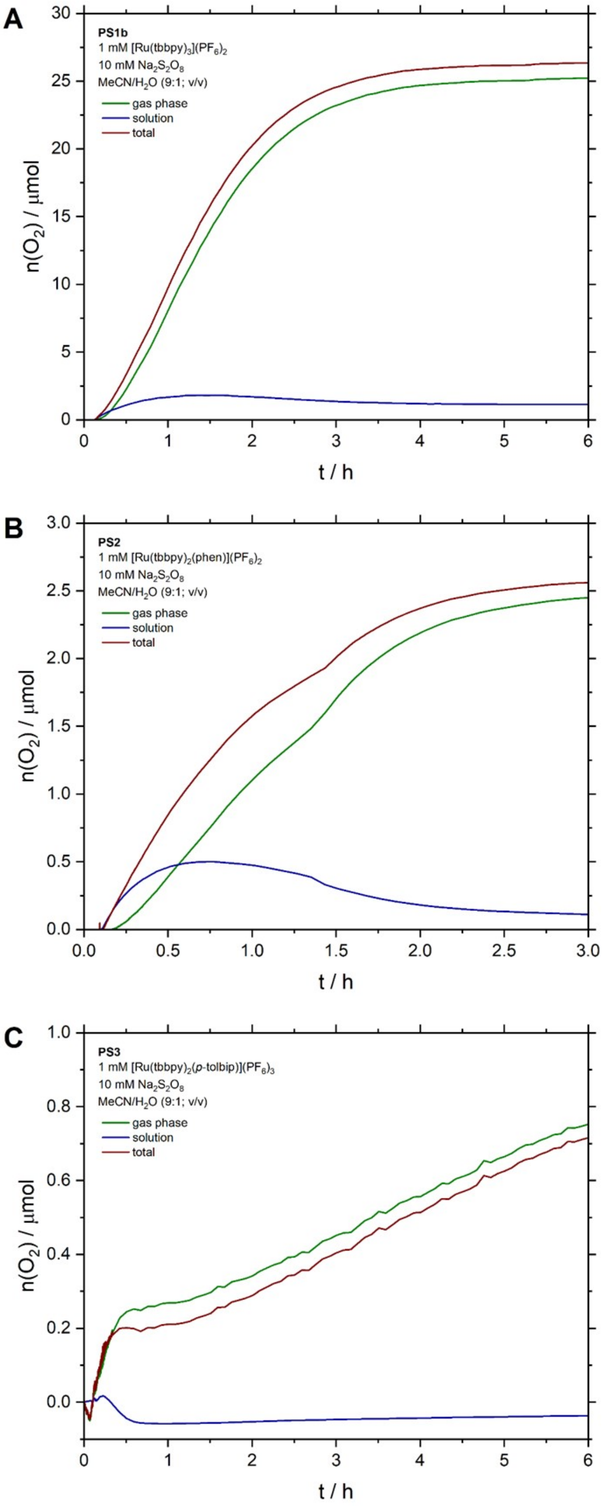

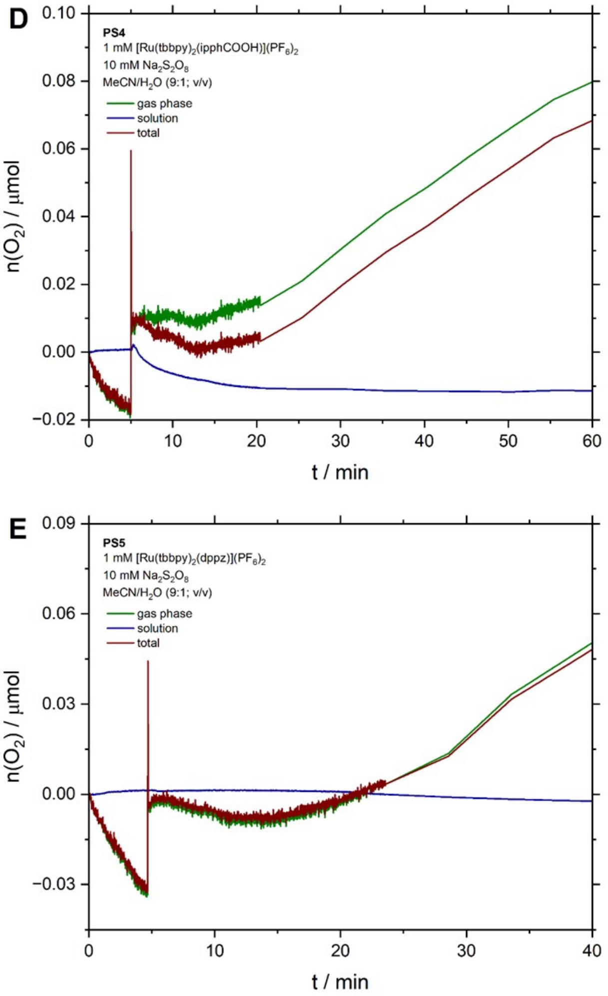

Figure S12: Light-driven OER profile in the gas phase (green), in solution (blue) and in total (red) using various ruthenium polypyridyl-based PS (1 mM) and $Na_2S_2O_8$ (10 mM) in MeCN/H_2O (9:1, v/v), as well as LED light (λ_{max} = 470 nm, power density: *ca*. 50 mW cm^{-2}): **A)** [Ru(tbbpy)$_3$](PF$_6$)$_2$ (PS1b): Slightly increased O_2 evolution upon irradiation compared to the prototype system with [Ru(bpy)$_3$](PF$_6$)$_2$ (PS1a). **B)** [Ru(tbbpy)$_2$(phen)](PF$_6$)$_2$ (PS2): Significantly reduced O_2 evolution upon irradiation. **C)** [Ru(tbbpy)$_2$(*p*-tolbip)](PF$_6$)$_3$ (PS3): Strongly reduced O_2 evolution upon irradiation. **D)** [Ru(tbbpy)$_2$(ipphCOOH)](PF$_6$)$_2$ (PS4): Negligible O_2 evolution upon irradiation. **E)** [Ru(tbbpy)$_2$(dppz)](PF$_6$)$_2$ (PS5): Negligible O_2 evolution upon irradiation.

10. Structural characterization data for ipphCOOH and PS4

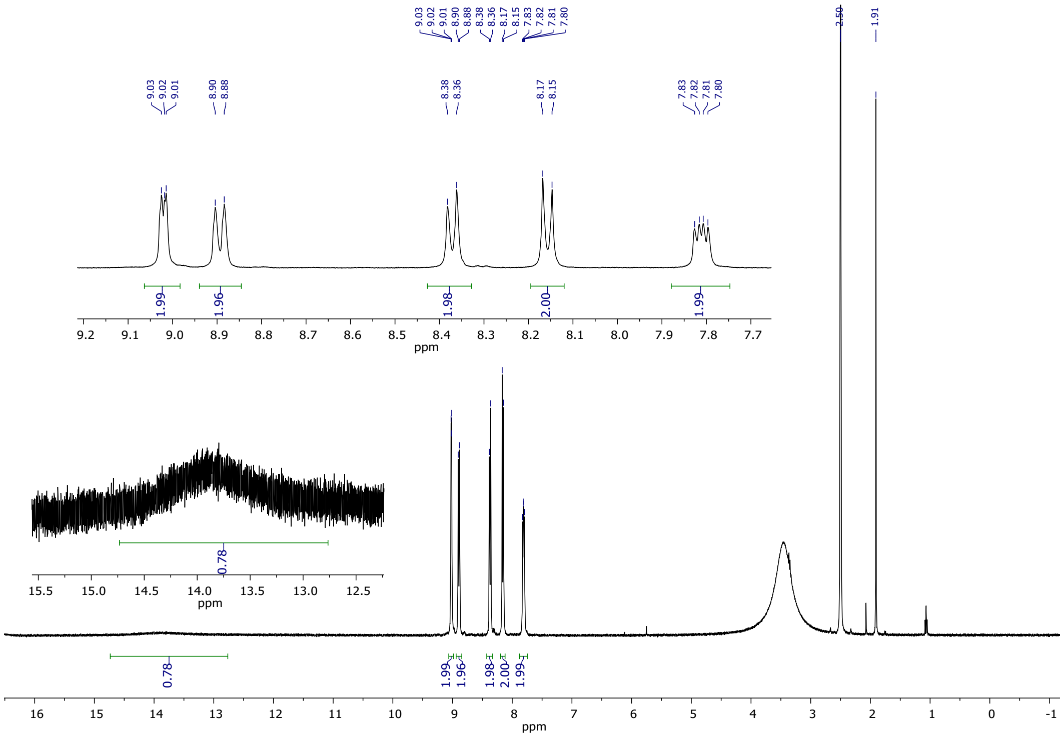

Figure S13: ^{1}H-NMR spectrum of ipphCOOH in DMSO-d_6 at room temperature; the peak at 1.91 ppm can be assigned to residual acetic acid.

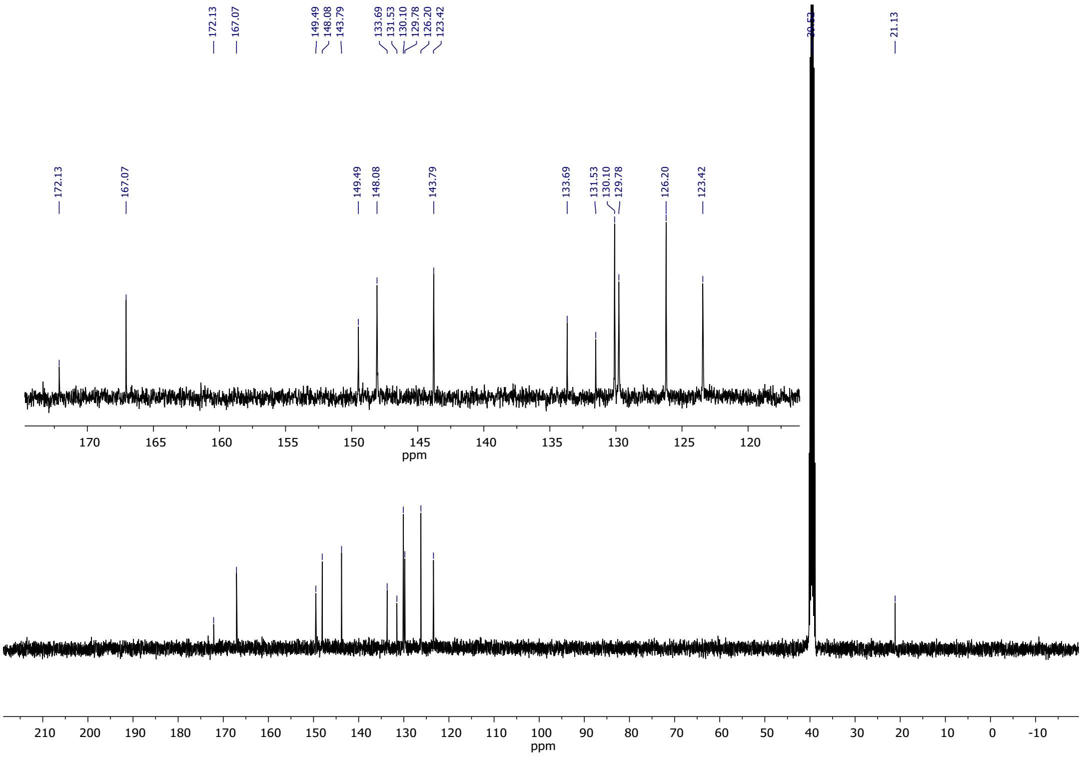

Figure S14: ^{13}C-NMR spectrum of ipphCOOH in DMSO-d_6 at room temperature; the peak at 21.13 ppm can be assigned to residual acetic acid. Only eleven of potential twelve signals between 100 and 200 ppm are observed, indicating peak overlap in one case.

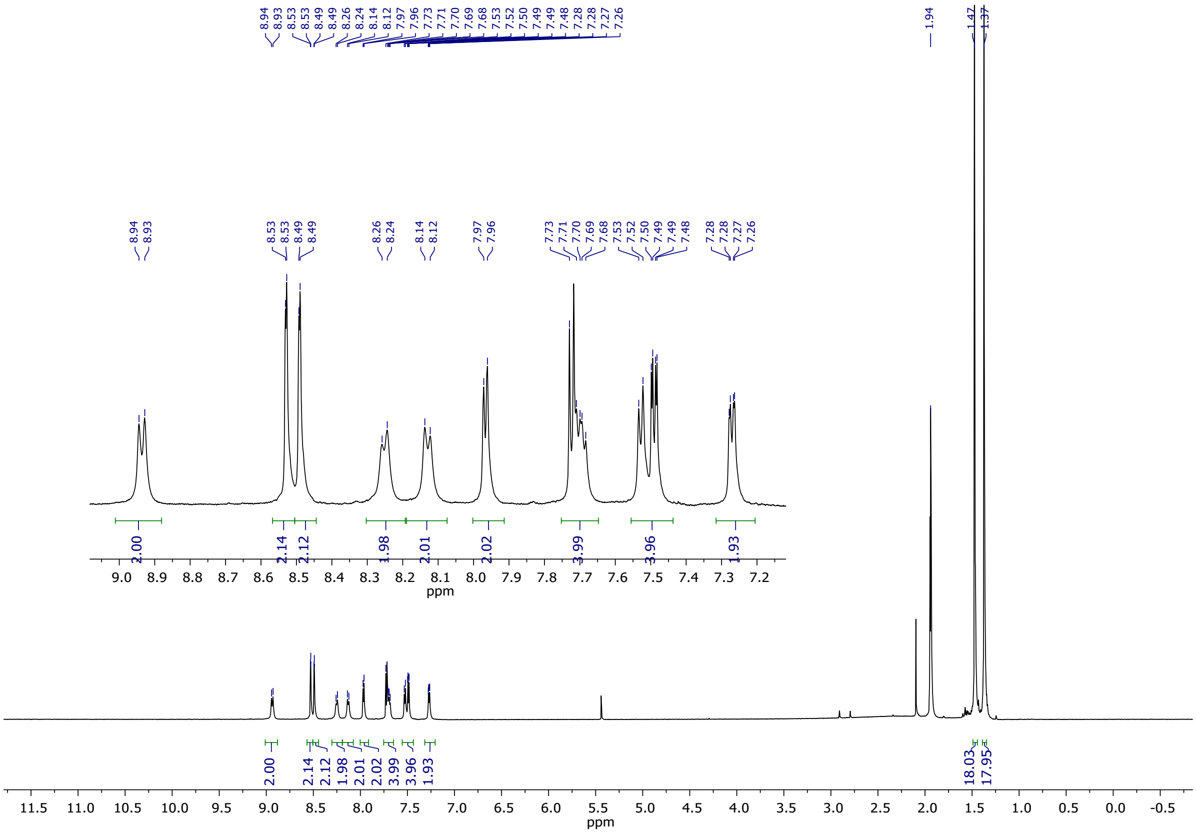

Figure S15: ^{1}H-NMR spectrum of [Ru(tbbpy)$_2$(ipphCOOH)](PF$_6$)$_2$ in MeCN-d$_3$ at 340 K.

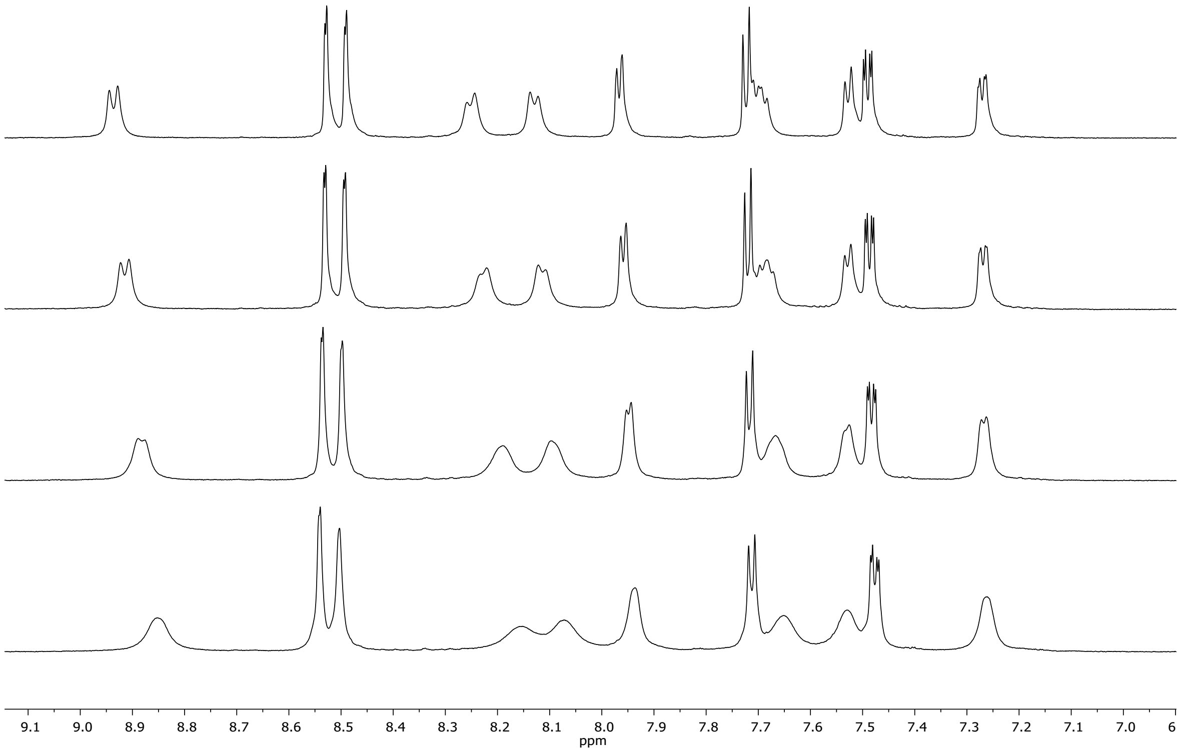

Figure S16: Series of *T*-dependent ^{1}H-NMR spectra of [Ru(tbbpy)$_2$(ipphCOOH)](PF$_6$)$_2$ in MeCN-d$_3$. Temperatures from top to bottom: 340 K, 330 K, 315 K, 300 K.

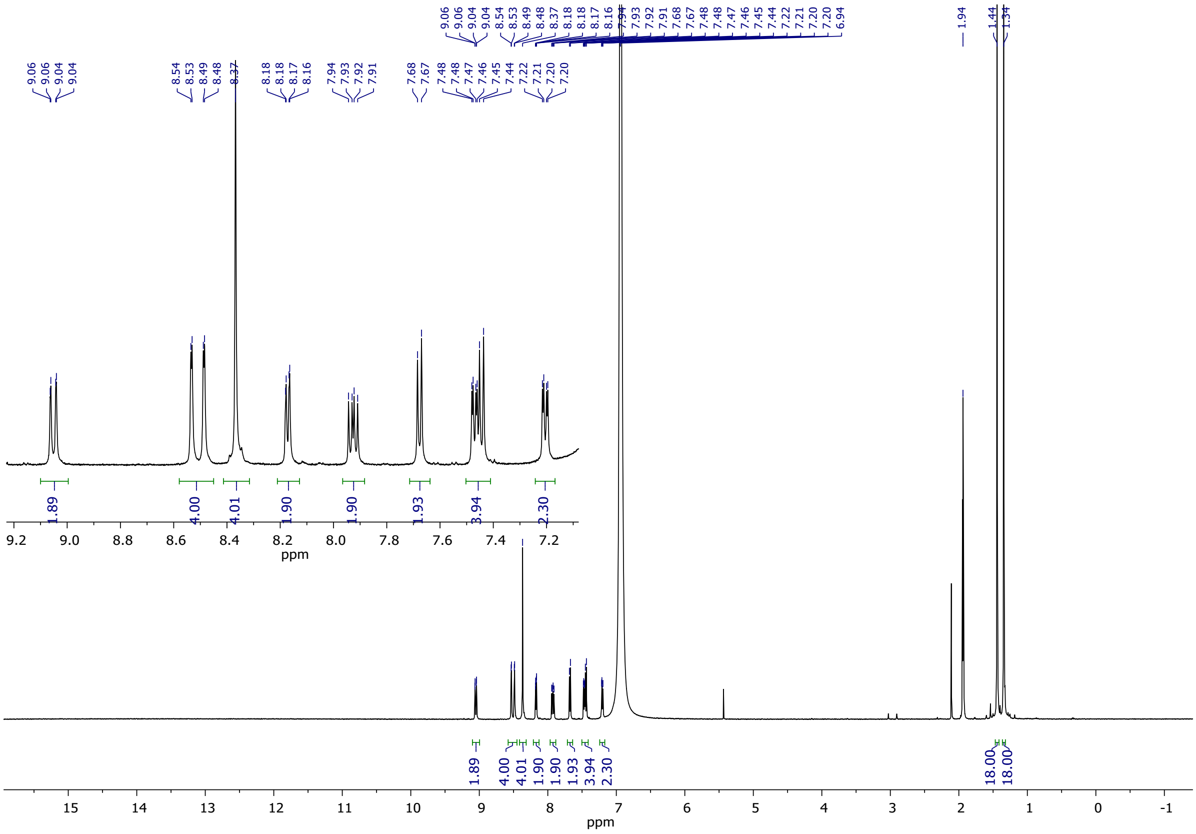

Figure S17: ^{1}H-NMR spectrum of [Ru(tbbpy)$_2$(ipphCOOH)](PF$_6$)$_2$ in MeCN-d$_3$ at room temperature in the presence of a small amount TFA-d.

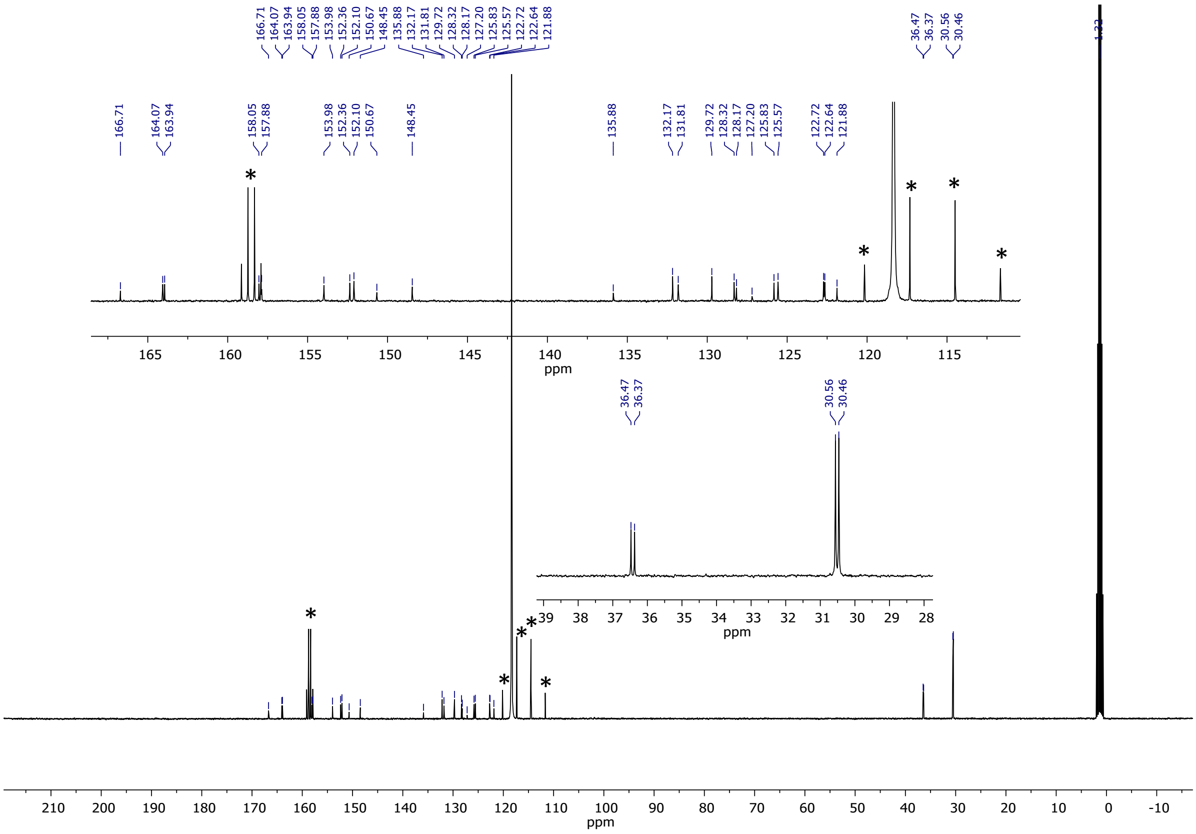

Figure S18: ^{13}C-NMR spectrum of [Ru(tbbpy)$_2$(ipphCOOH)](PF$_6$)$_2$ in MeCN-d$_3$ at room temperature with some TFA added to improve the spectrum. Peaks assigned with an asterisk are due to TFA (see Figure S19).

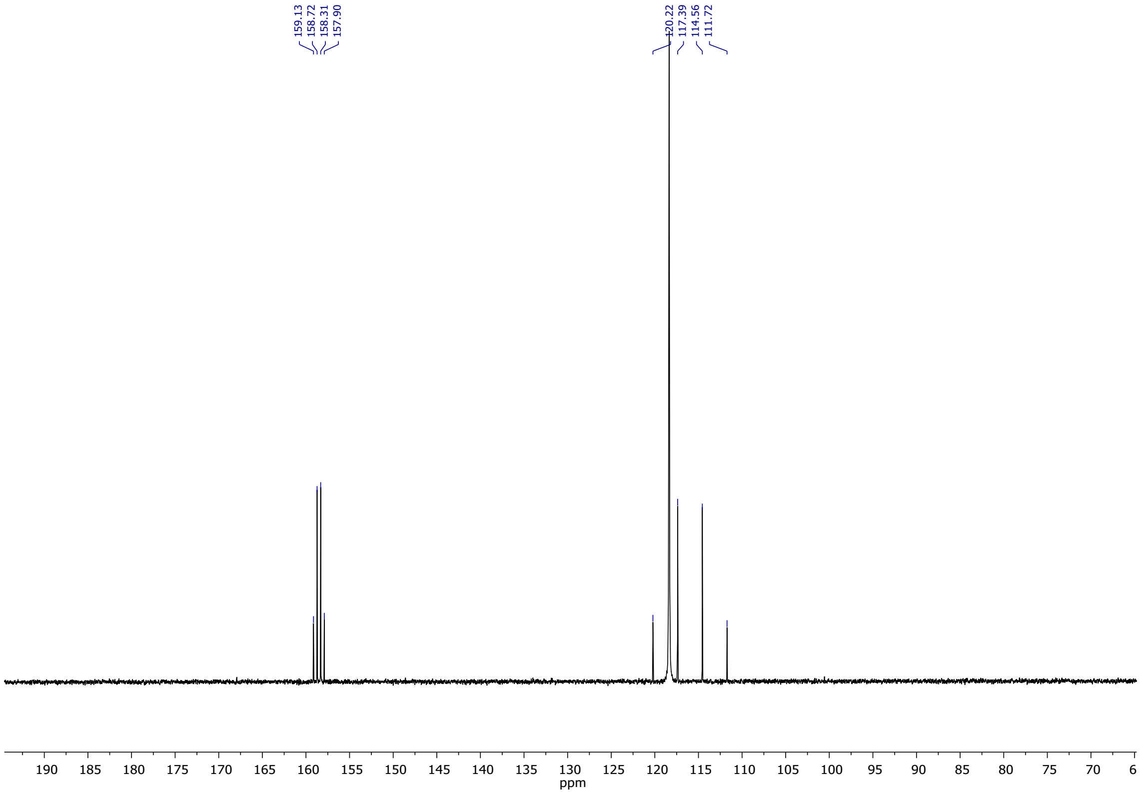

Figure S19: ^{13}C-NMR spectrum of TFA in MeCN-d_3 at room temperature.

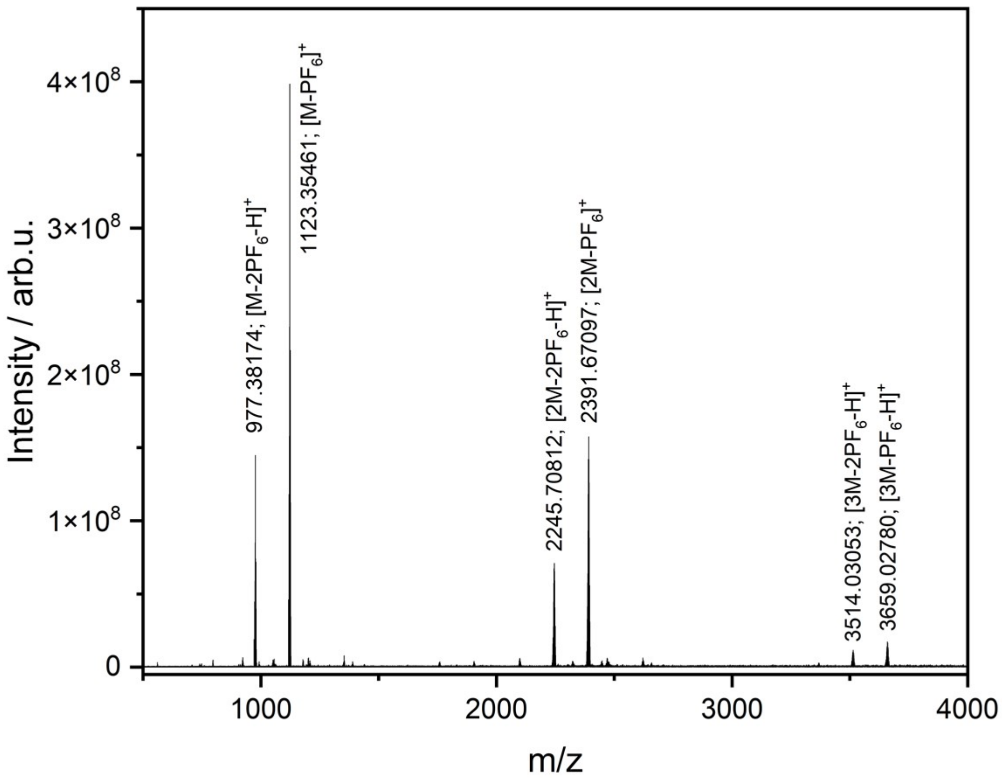

Figure S20: Full high-resolution MALDI-MS spectrum of [Ru(tbbpy)$_2$(ipphCOOH)](PF$_6$)$_2$ with peak assignments and detailed m/z values of the respective highest peak.

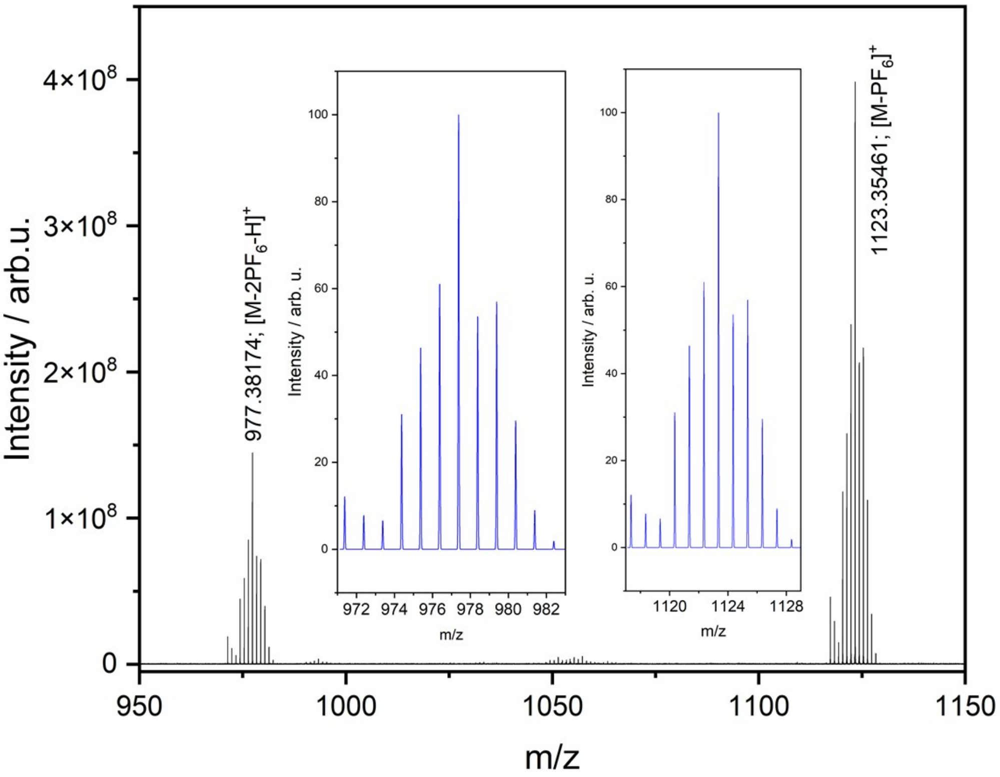

Figure S21: High-resolution MALDI-MS spectrum of [Ru(tbbpy)$_2$(ipphCOOH)](PF$_6$)$_2$ in the range of 950-1150 m/z depicting the experimentally obtained MS peaks of highest intensity as well as modelled MS peaks as insets (blue spectra).

11. Control experiment in purely aqueous media

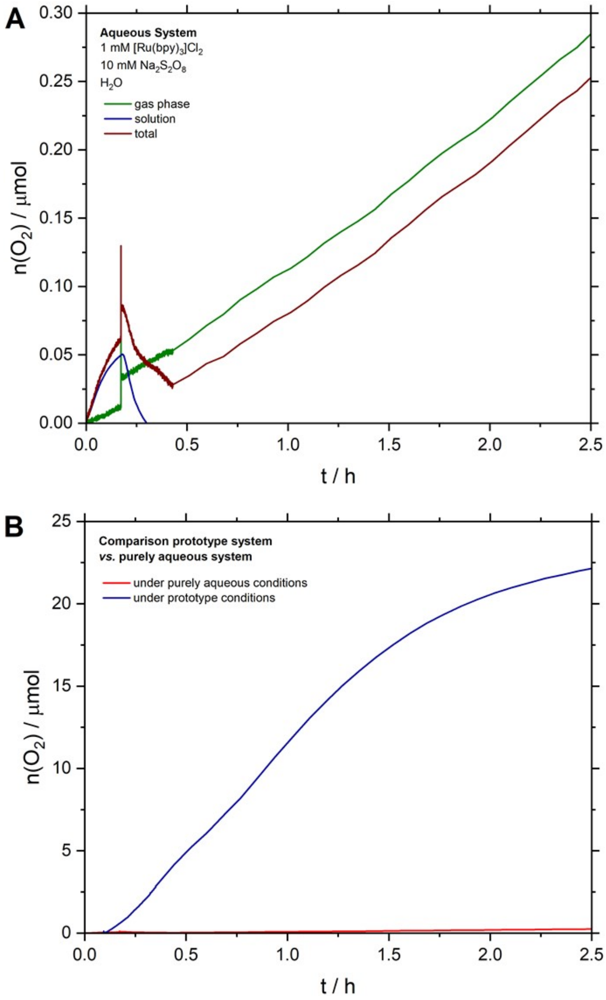

Figure S22: Control experiment: **A)** Light-driven OER profile in the gas phase (green), in solution (blue) and in total (red) for the control experiment in purely aqueous media using the OER system with $[Ru(bpy)_3]Cl_2$ (1 mM) and $Na_2S_2O_8$ (10 mM) in H_2O; LED light (λ_{max} = 470 nm, power density: *ca*. 50 mW cm^{-2}). **B)** Comparison of the total amounts of O_2 evolved in light-driven OER under purely aqueous conditions with $[Ru(bpy)_3]Cl_2$ (1 mM) and $Na_2S_2O_8$ (10 mM) in H_2O (red) and under the prototype conditions reported with $[Ru(bpy)_3](PF_6)_2$ (1 mM) and $Na_2S_2O_8$ (10 mM) in $MeCN/H_2O$ (9:1, v/v) using LED light (λ_{max} = 470 nm, power density: *ca*. 50 mW cm^{-2}) (blue). Reduced O_2 evolution indicates that the underlying processes of light-induced PS degradation and formation of catalytically active ruthenium dimer species are significantly faster under the reported conditions for the OER prototype system.

12. Literature

1 C. Wang, L. Lystrom, H. Yin, M. Hetu, S. Kilina, S. A. McFarland and W. Sun, *Dalton Trans.*, 2016, **45**, 16366–16378.

2 S. Rau, B. Schäfer, A. Grüßing, S. Schebesta, K. Lamm, J. Vieth, H. Görls, D. Walther, M. Rudolph, U. W. Grummt and E. Birkner, *Inorganica Chim. Acta*, 2004, **357**, 4496–4503.

3 M. Lämmle, B. Bagemihl, D. Nauroozi, L. Petermann, A. Pannwitz and S. Rau, *ChemPhotoChem*, 2022, **6**, e202200053.

4 A. K. Mengele, D. Weixler, A. Chettri, M. Maurer, F. L. Huber, G. M. Seibold, B. Dietzek, B. J. Eikmanns and S. Rau, *Chem. Eur. J.*, 2021, **27**, 16840–16845.

5 F. L. Huber, S. Amthor, B. Schwarz, B. Mizaikoff, C. Streb and S. Rau, *Sustain. Energy Fuels*, 2018, **2**, 1974–1978.

6 U. S. Akhtar, E. L. Tae, Y. S. Chun, I. C. Hwang and K. B. Yoon, *ACS Catal.*, 2016, **6**, 8361–8369.

7 Z. Y. Chen, D. Persson and C. Leygraf, *J. Electrochem. Soc.*, 2005, **152**, B526–B533.